ACS NANO

www.acsnano.org

ARTICLE

Simple Synthesis of Nanocrystalline Tin Sulfide/N-Doped Reduced Graphene Oxide Composites as Lithium Ion Battery Anodes

Duck Hyun Youn,[†] Shannon K. Stauffer,[‡] Penghao Xiao,[‡] Hunmin Park,[§] Yejin Nam,[†] Andrei Dolocan,[∥] Graeme Henkelman,[‡] Adam Heller,[†] and C. Buddie Mullins*[,†,∥]

[†]Department of Chemical Engineering and Department of Chemistry, Center for Electrochemistry, University of Texas at Austin, 1 University Station, C0400 Austin, Texas 78712-0231, United States

[‡]Department of Chemistry and the Institute for Computational Engineering and Sciences, University of Texas at Austin, Austin, Texas 78712-0165, United States

[§]Department of Chemical Engineering, Pohang University of Science and Technology (POSTECH), Pohang, 790-784, South Korea

[∥]Texas Materials Institute, University of Texas at Austin, Austin, Texas 78712-1591, United States

Supporting Information

ABSTRACT: **Composites of nitrogen-doped reduced graphene oxide (NRGO) and nanocrystalline tin sulfides were synthesized, and their performance as lithium ion battery anodes was evaluated. Following the first cycle the composite consisted of Li_2S/Li_xSn/NRGO. The conductive NRGO cushions the stress associated with the expansion of lithiation of Sn, and the noncycling Li_2S increases the residual Coulombic capacity of the cycled anode because (a) Sn domains in the composite formed of unsupported SnS_2 expand only by 63% while those in the composite formed of unsupported SnS expand by 91% and (b) Li percolates rapidly at the boundary between the Li_2S and Li_xSn nanodomains. The best cycling SnS_2/NRGO-derived composite retained a specific capacity of 562 mAh g^{-1} at the 200th cycle at 0.2 A g^{-1} rate.**

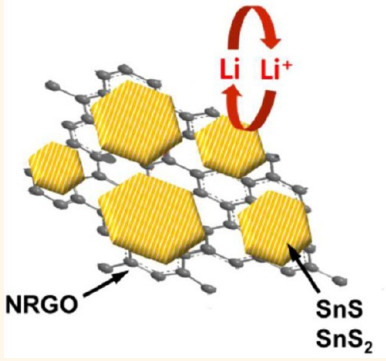

KEYWORDS: *SnS, SnS_2, reduced graphene oxide, lithium ion battery anode*

Lithium ion batteries (LiBs) are the predominant power source for portable devices and electric vehicles due to their high efficiency and high energy density.[1] Currently used graphite anodes with a low theoretical capacity of 372 mAh g^{-1} are insufficient to satisfy the demand for increasing energy and power densities. Therefore, it is necessary to develop efficient anode materials for LiBs possessing high lithium capacity with excellent rate capability and cycling stability.[2] Recently, intensive research efforts have focused on developing LiB anode candidates including group IV elements, metal oxides, and metal chalcogenides.[3−5] Transition metal sulfides are considered as promising anode materials to replace the current graphite anode due to their higher capacity through a conversion and alloying reaction.[6−8] The sulfides of tin, SnS and SnS_2, have been intensively studied as electroactive components for Li-ion battery anodes because of their high theoretical capacity (782 mAh g^{-1} for SnS and 645 mAh g^{-1} for SnS_2), low cost, earth abundance, and low toxicity.[7,9] Additionally, in their initial reduction half-cycle, they are irreversibly converted to Li_2S and Sn ($SnS_x + 2xLi^+ + 2xe^- \rightarrow Sn + xLi_2S$, $x = 1, 2$); at the relevant potentials, only Sn is lithiated/delithiated. The Li_2S domains are thought to buffer the stress associated with the expansion/shrinkage of the lithiation/delithiation of Sn, slowing the fading of capacity *versus* that of pure Sn.[10] Still, the pulverization and subsequent capacity fading of tin sulfide-based electrodes during the cycling can be improved.[11]

To enhance the cycling performance and rate capability, one effective approach is to fabricate nanostructured tin sulfides. The stress relaxation of nanostructured materials is faster than that of materials having a substantial crystalline domain size, and the diffusion distance of lithium ions into nanocrystallites is shorter; thus nanostructured SnS and SnS_2 show enhanced cycling performance and rate capability over large-grained tin sulfide materials.[12,13] Compounding with conductive carbon is another approach to improve the performance of tin sulfides. Carbon materials including carbon blacks, CNTs, or graphene not only provide a high electrical conductivity to the tin sulfides

Received: June 24, 2016
Accepted: November 22, 2016
Published: November 22, 2016

DOI: 10.1021/acsnano.6b04214
ACS Nano 2016, 10, 10778−10788

but also act as a cushion to buffer the volume change during lithiation/delithiation.[14,15] The integration of graphene with tin sulfides has been previously applied to the LiB anode due to favorable properties such as large surface area, high electrical conductivity, and chemical stability,[16−21] and these anodes show enhanced cycling stability and rate performance compared to the bare SnS or SnS_2 electrodes. In addition, nitrogen-doped graphenes have been employed as a support for tin sulfides as well as other anode materials.[3,5,20] The composites made with nitrogen-doped graphene exhibited further enhanced performance compared with composites made with undoped graphene. Nitrogen-doped graphene can retain the favorable properties of graphene (stated above) and gain additional favorable properties such as increased electrical conductivity for faster charge transfer and induced defect sites for more lithium storage.[3,5,20] Thus, combining nanostructured tin sulfides with a nitrogen-doped graphene would be an effective way to improve the performance of LiB anodes.

Here, we report a simple fabrication method involving SnS and SnS_2 particles with a nitrogen-doped reduced graphene oxide (NRGO) support, which presents several advantages: First, our synthetic method is phase selective and simple. A pure form of nanocrystalline SnS or SnS_2 is easily fabricated on NRGO from the same precursors by simply varying the annealing temperature. Also, no additional reduction step for graphene oxide (GO) is required owing to simultaneous reduction of GO by thermal annealing with the formation of tin sulfide nanocrystals. Furthermore, nitrogen doping of the RGO was also achieved simultaneously employing thiourea. Second, the electrochemical performance of the tin sulfides/NRGO composites is systematically compared, and the reasons for the performance differences were elucidated using computational simulations. Indeed, a comparison of electrochemical performances between orthorhombic SnS and hexagonal SnS_2 as LiB anode materials is rare.[22] Here we provide physicochemical and electrochemical information regarding the SnS_2/NRGO and SnS/NRGO composites to the research community. Third, our SnS_2/NRGO electrode showed promising cycling stability compared to other tin sulfide-based electrodes. It retained a specific capacity of 562 mAh g^{-1} at the 200th cycle at 0.2 A g^{-1}. Thus, the present work could serve as a guideline for selecting and designing a transition metal sulfide based electrode for the LiB anode.

RESULTS AND DISCUSSION

One-Step Synthesis and Characterization of the Nanocrystalline SnS_x/NRGO Composites. The one-step synthesis of nanocrystalline composites of tin sulfides and nitrogen-doped reduced graphene oxide composites from $SnCl_4$, thiourea, and graphene oxide is illustrated in Figure 1. The reactions between the Sn precursor and thiourea were investigated by infrared (IR) spectroscopy as illustrated in Figure S1a. The $SnCl_4$ reacts vigorously with ethanol, generating the Sn ethoxide, which further combines with thiourea to form a gel-like Sn-thiourea complex (Figure S1b). As seen in Figure S1a, after $SnCl_4$ was mixed with thiourea, a red shift of the C═S stretching peak (from 729.3 to 701.8 cm^{-1}) and a blue shift of the C−N stretching peak are observed compared to the pristine thiourea. These results indicate changes in the double-bond characteristics of C═S and C−N bonds, respectively, suggesting that the sulfur atom in thiourea coordinates with the metal ion to yield a Sn-thiourea complex.[23,24] In the presence of GO, the C═S and C−N

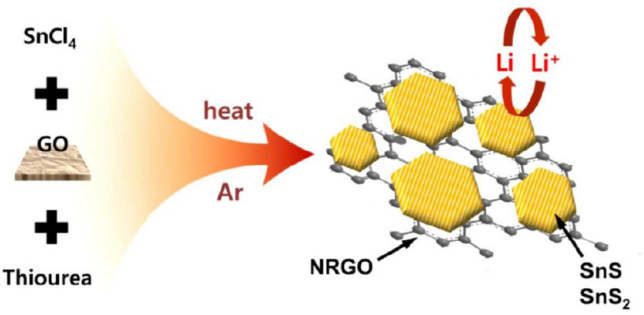

Figure 1. One-step synthesis of nanocrystalline SnS/NRGO and SnS_2/NRGO composites.

peaks were located similarly to Sn-thiourea, revealing the same reaction takes place on the GO layers. In addition, the C═O stretching peak is shifted from 1625.7 to 1591.6 cm^{-1} compared to pristine GO, which indicates an interaction between GO with the Sn-thiourea complex (Sn-thiourea-GO complex). When the composite is annealed at 450 °C, the tin sulfide is nanocrystalline SnS_2; when annealed at 650 °C, the tin sulfide is nanocrystalline SnS. During the synthetic process, the graphene oxide not only is reduced by thermal annealing[25] but is also heavily doped by nitrogen from thiourea. Furthermore, oxygen-containing functional groups on GO attract the metal precursor, as evidenced by IR results, and thus the tin sulfide nanocrystals grow exclusively on the NRGO sheets.[26] In our synthetic method, it is worth pointing out that two different tin sulfides/NRGO composites (and their bare forms) were prepared from the same precursors, enabling a fair performance comparison between them. Furthermore, the final crystal phases were easily controlled just by varying temperature. Further, no additional loading of active phase or changes to the reduction process for GO is required, suggesting the simplicity of the synthetic method.

Figure S2 shows the XRD patterns of the nanocrystallites. After processing at 450 °C, the XRD pattern is consistent with that of hexagonal SnS_2 (JCPDS 023-0677), a layered transition metal disulfide, where the tin atoms are sandwiched between layers of hexagonally close packed sulfur atoms.[22] Other impurity peaks including Sn metal or tin oxide were not detected. When the processing temperature is raised to 550 °C, part of the sulfur diffuses out, resulting in less intense SnS_2 peaks.[27] At 650 °C only orthorhombic SnS remains, and its reflections correspond to the reference spectra (JCPDS 014-0620). In this study, the SnS_2 and SnS annealed at 450 and 650 °C, respectively, were used as representative samples, and their composites with the NRGO were also annealed at 450 °C for the SnS_2/NRGO and 650 °C for the SnS/NRGO. Figure 2 shows the corresponding X-ray diffraction (XRD) patterns of the composites, which are consistent with the reference XRD patterns stated above. GO displayed a characteristic peak at *ca.* 11° from the (002) planes. The absence of the GO peak at 11° in the SnS_2/NRGO and the SnS/NRGO composites indicates the reduction of GO during the annealing step,[28] which will be further confirmed by various other characterization techniques.

Figure 3 shows scanning electron microscopy (SEM) images of the nanocrystallites and their NRGO composites. In the absence of NRGO, the SnS_2 and SnS nanocrystallites agglomerate, with the SnS_2 nanocrystallites forming 0.1 μm to multi-μm-diameter clusters (Figure 3a); because of the higher processing temperature of SnS, its nanocrystallites agglomerate even more, growing to greater than 10 μm

DOI: 10.1021/acsnano.6b04214
ACS Nano 2016, 10, 10778−10788

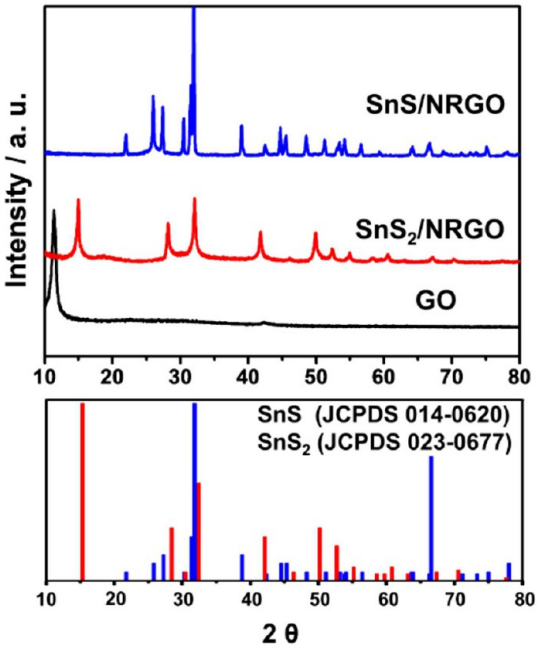

Figure 2. XRD patterns of the reference (bottom) and the synthesized SnS/NRGO, SnS_2/NRGO, and GO (top).

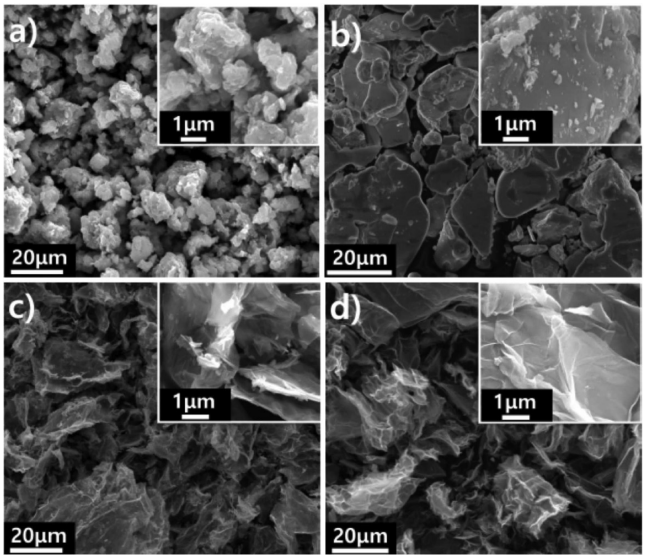

Figure 3. SEM images of (a) SnS_2, (b) SnS, (c) SnS_2/NRGO, and (d) SnS/NRGO.

particles (Figure 3b). Figure 3c and d show that the NRGO is wrinkled and that the SnS_2 or SnS nanoparticles grow exclusively on the NRGO; there are no nanoparticles elsewhere. Energy dispersive spectroscopic (EDS) mapping of the SnS_2/NRGO and SnS/NRGO composites (Figures S3a–d and S4a–d) shows that the tin, sulfur, and the carbon are homogeneously distributed on the NRGO sheets. The Sn:S atomic ratio in the SnS_2/NRGO composite is 1.00:1.78 (Figure S3e); it is 1.00:0.95 in the SnS/NRGO composite (Figure S4e).

The transmission electron microscopy (TEM) images of Figure 4 confirm the growth of large SnS_2 and SnS crystals in the absence of NRGO (Figure 4a and b) and restriction of their crystal growth (resulting in a smaller size) in the presence of NRGO (Figure 4c and d). The TEM images also show the characteristic layered structure of SnS_2 with an interlayer

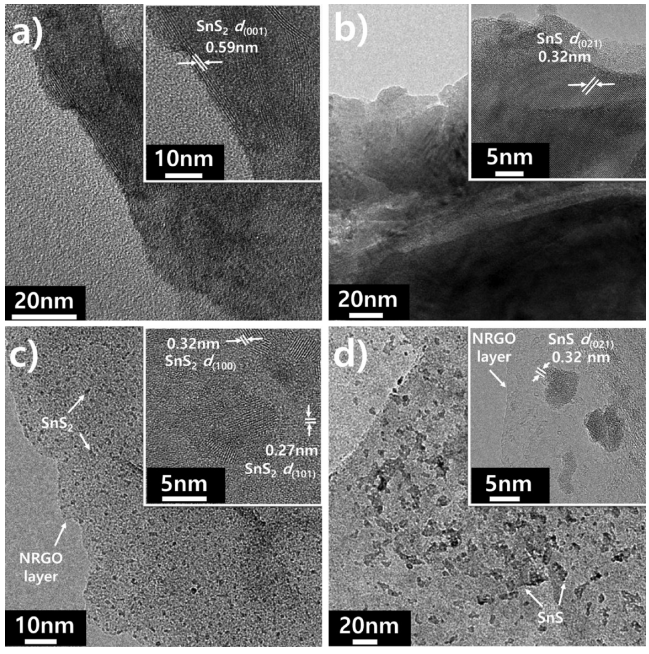

Figure 4. TEM images of (a) SnS_2, (b) SnS, (c) SnS_2/NRGO, and (d) SnS/NRGO.

d(001) distance of 0.59 nm (Figure 4a); for SnS, the images show a d(021) lattice spacing of 0.32 nm (Figure 4b). The 3–10 nm diameter SnS_2 nanocrystallites are uniformly dispersed on the wrinkled NRGO sheets (Figure 4c); their 0.32 and 0.27 nm lattice spacings (inset of Figure 4c) correspond to the d(100) and d(101) planes of SnS_2.[16] The size of the also uniformly distributed SnS nanocrystals on the NRGO sheets is 5–15 nm (Figure 4d), and their 0.32 nm lattice spacing corresponds to that of the d(021) plane. The graphene-like structure of NRGO is evident from Figure S5, where the 0.34 nm spacing of the RGO d(002) plane is clearly observed with the d(100) plane of SnS_2 (Figure S5a) and the d(040) plane of SnS (Figure S5b), confirming the reduction of the graphene oxide. Overall, the TEM data show that the NRGO mediated the growth of the tin sulfide. In the absence of NRGO the tin sulfide nanocrystals aggregate, while in its presence they do not. The oxygen-containing functional groups on GO attract the metal precursor, and thus the tin sulfide nanocrystals are grown on the NRGO layer selectively. Apparently, a strong coupling between the metal sulfide nanocrystals and the NRGO prevents their aggregation[29] and improves their accessibility in their electrochemical reaction with Li^+.

In the Raman spectra of Figure 5a the D peak at 1350 cm^{-1} is attributed to a defect-induced breathing mode of sp^2 rings, while the G peak at 1590 cm^{-1} originates from first-order scattering of the E_{2g} mode of sp^2 domains.[30] The numerical values in the figure are the intensity ratios of the D and G peaks (I_D/I_G ratios). The I_D/I_G ratio is a measure of the degree of disorder; an increase in I_D/I_G implies restoration of sp^2 carbon and smaller sp^2 domains upon reduction of GO.[30−32] Thus, the higher I_D/I_G ratio of SnS_2/NRGO (1.02) and SnS/NRGO (1.12) *versus* that of GO (0.85) shows that the GO is indeed reduced to NRGO during the annealing step.

Chemical states of the prepared samples are examined by X-ray photoelectron spectra (XPS) in Figure 5b–d. In the Sn 3d spectra (Figure 5b), the 487.3 and 495.6 eV peaks for the SnS_2 and the SnS_2/NRGO composite are assigned to Sn $3d_{5/2}$ and

DOI: 10.1021/acsnano.6b04214
ACS Nano 2016, 10, 10778–10788

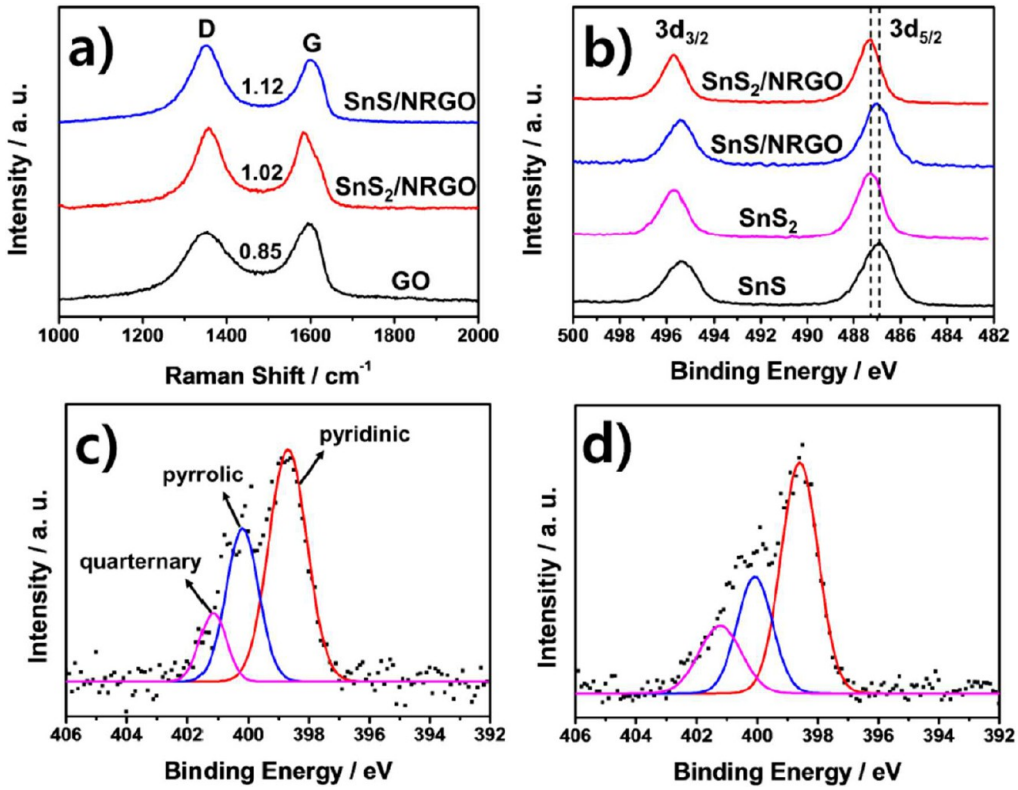

Figure 5. (a) Raman spectra of GO, SnS_2/NRGO, and SnS/NRGO. (b) XPS spectra of the prepared samples for Sn 3d. N 1s spectra of (c) SnS_2/NRGO and (d) SnS/NRGO.

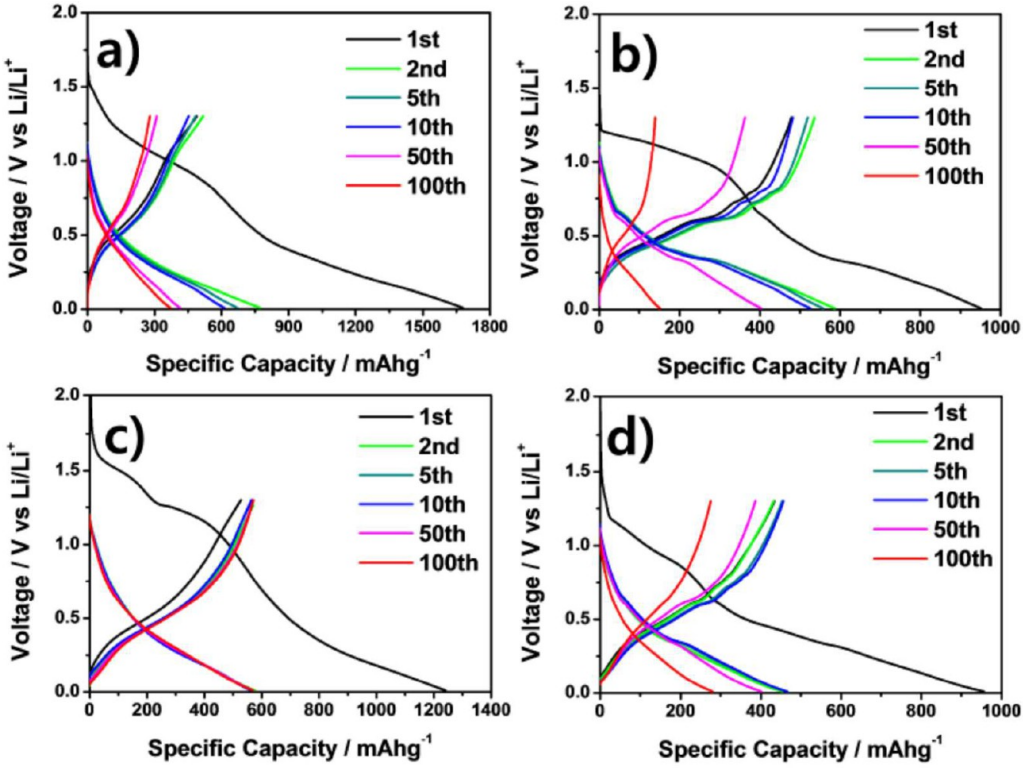

Figure 6. Potential dependence of the specific capacity of the (a) SnS_2, (b) SnS, (c) SnS_2/NRGO, and (d) SnS/NRGO.

$3d_{3/2}$, respectively, which corresponds to Sn^{4+}, while the corresponding peaks at 486.8 and 495.4 eV in the SnS and the SnS/NRGO composite are assigned to the lower oxidation state of Sn^{2+}. The 401.1, 400.2, and 398.6 eV peaks of the N 1s spectra of the SnS_2/NRGO (Figure 5c) and SnS/NRGO (Figure 5d) are assigned respectively to quarternary, pyrrolic,

DOI: 10.1021/acsnano.6b04214
ACS Nano 2016, 10, 10778−10788

and pyridinic nitrogens. The nitrogen content of the resulting SnS_2/NRGO composite is 10.4 atom %, and that of the resulting SnS/NRGO composite is 11.9 atom %. In general, the nitrogen-doping improves the electronic conductivity,[33] reducing the internal resistance of the resultant lithium anodes. Also, the extended defect sites and vacancies could facilitate more insertion of Li^+ as the cycle number increases, resulting in good cycling stability.[5] In this work, the nitrogen doping of the RGO is simultaneously achieved by using thiourea, which acts as a sulfur (for tin sulfide crystallization) and nitrogen source (nitrogen doping of RGO) at the same time. Figure S6 shows the C 1s spectra of SnS_2/NRGO, SnS/NRGO, and GO. The pristine GO has oxygen-containing (*e.g.*, hydroxyl, carboxyl, and epoxy) functions, evident from the broad 280−290 eV peaks of Figure S6a.[26] In SnS_2/NRGO (Figure S6b) and SnS/NRGO (Figure S6c) the intensities of these peaks are significantly decreased, consistent with the reduction of GO to NRGO. The TEM, Raman, and XPS results clearly demonstrate the reduction of GO *via* the synthetic procedure.

Thermogravimetric analysis was carried out from 30 to 1000 °C at the rate of 10 °C/min under an air atmosphere. The weight loss of the composites is mainly attributed to the removal of the NRGO (carbon decomposition to carbon dioxide) and the oxidation of tin sulfides to tin oxide. By assuming that the final product of the TGA heating is SnO_2, the contents of SnS_2 in the SnS_2/NRGO and SnS in the SnS/NRGO were determined to be 50.5 and 48.8 wt % based on the equation shown in Figure S7. A similar content of tin sulfide nanocrystals in the composites is necessary for a fair performance comparison.

Electrochemical Characteristics. Electrodes made with unsupported and NRGO-supported SnS_2 and SnS were galvanostatically cycled at a 0.2 A g^{-1} rate, between a constant lower potential limit of 0.01 V *versus* Li^+/Li and a constant upper potential limit of 1.30 V. The voltage profiles of the first, second, 10th, 50th, and 100th cycles of the four electrodes are shown in Figure 6. The first discharge and charge capacities of the SnS_2 were 1677 and 569 mAh g^{-1}, corresponding to an initial Coulombic efficiency of 34% (Figure 6a). The low initial efficiency (*ca.* 30%) of the SnS_2 electrodes has been previously reported[34] and is mainly ascribed to the initial irreversible lithium consumption and formation of the solid electrolyte interphase (SEI). The plateaus at *ca.* 1.2 V and below 0.5 V during the first discharge scan correspond to the decomposition of SnS_2 (into Sn and Li_2S) and the formation of Li−Sn alloys, which is consistent with a previous report.[35] The Li_2S matrix generated during the first discharge remained throughout the cycles that followed with a inactive buffer layer surrounding Sn domains.[36] Note that the Li_2S is an inert phase in the present potential range.[9,37] The gradual decrease in the capacity of the SnS_2 electrode was observed with a capacity of 370 mAh g^{-1} at the 100th cycle. For the SnS electrode, the first discharge and charge capacities are 950 and 478 mAh g^{-1} with an initial Coulombic efficiency of 50% (Figure 6b). The plateau at *ca.* 1.25 V and below 0.5 V during the first cathodic scan represents the reduction of SnS (into Sn and Li_2S) and the SEI formation.[9,20] The SnS shows a rapid capacity decay with a capacity of 151 mAh g^{-1} at the 100th cycle, exhibiting poorer cycling stability compared to the SnS_2 electrode. The SnS_2/NRGO electrode shows similar lithiation/delithiation behavior to the SnS_2, with the first discharge and charge capacities of 1240 and 588 mAh g^{-1} (the initial Coulombic efficiency of 47%). In stark contrast to the bare SnS_2, the voltage profiles of the SnS_2/NRGO were largely not changed from the second cycle, with a reversible capacity of 580 mAh g^{-1} at the 100th cycle, implying an excellent cycling stability (Figure 6c). The first discharge and charge capacities of the SnS/NRGO were 955 and 434 mAh g^{-1}, corresponding to an initial Coulombic efficiency of 45% (Figure 6d). It shows a capacity of 279 mAh g^{-1} at the 100th cycle, showing improved cycling stability relative to the SnS, but inferior to the SnS_2/NRGO.

Figure S8 shows the cyclic voltammograms (CVs) of the electrodes at a scan rate of 0.1 mV s^{-1}. For the SnS_2 and the SnS_2/NRGO electrodes (Figure S8a and c), the peak at about 1.2 V in the first cathodic scan is assigned to the formation of the SEI layer and the decomposition of SnS_2 into metallic Sn and Li_2S, which is responsible for the initial irreversible capacity loss. Another cathodic peak at around 0.1 V and the anodic peak at 0.6 V in the first scan are attributed to the redox pair of alloying and dealloying of Sn metal.[35,38] The CV curves of the SnS and the SnS/NRGO electrodes (Figure S8b and d) show the cathodic peak at 1.1 V during the first scan, which is due to the SEI formation and the decomposition of SnS into Sn and Li_2S. Another peak at about 0.6 V in the scan is assigned to the formation of the Li_xSn alloy with the x range of 0.57−1.0. The peak at around 0.2 V originates from the alloying process of Li_xSn with a higher x range of 1.0−4.4.[19,39] For the anodic scan, four peaks are observed at 0.47−0.8 V, corresponding to the dealloying reaction, indicating the discrete nature of the alloying and dealloying process.

In order to obtain direct evidence of the formation of the Li_xSn alloy and Li_2S structure after the first discharge, a representative cycled SnS_2/NRGO electrode was analyzed by TEM. Figure S9a shows the TEM image of the SnS_2/NRGO electrode, where small black particles of 3.4 nm size are surrounded by a gray matrix. The nanoparticles are Li_xSn alloys formed by the conversion and alloying reaction of the SnS_2 during lithiation. This structure was further confirmed by the STEM image (Figure S9b) and the corresponding EDS mapping images (Figure S9c−f). Like the TEM image in Figure S9a, white particles are surrounded by a gray layer in Figure S9b. As evidenced by the mapping images, the white particles are Li_xSn (Figure S9e) and the gray layer is Li_2S (Figure S9f). Note that detection of Li by EDS is restricted due to its low energy of characteristic radiation. The combined mapping image of Sn and sulfur clearly shows that Li_xSn particles are distributed in a Li_2S matrix (Figure S9c).

The TEM results are further supported by XRD and time-of-flight secondary ion mass spectrometry (TOF-SIMS) measurements. Figure S10a shows the XRD patterns of the SnS_2/NRGO electrode after first lithiation and delithiation. The Li_2S peaks were detected in both lithiated and delithiated states, indicating the existence of Li_2S during both the charging/discharging step. The TOF-SIMS depth profiles of the SnS_2/NRGO electrodes (negative secondary ion detection mode, Cs^+ sputtering) after first charge and discharge are shown in Figure S10b. The pristine SnS_2/NRGO electrode showed a virtually zero LiS^- signal (normalized to the Sn^- signal) throughout the analyzed depth. In contrast, the normalized LiS^- signals of both lithiated and delithiated SnS_2/NRGO exhibited strong, sharp peaks at the surface, suggesting a LiS-containing coating. These results indicate that the Sn species in the lithiated and delithiated electrodes are surrounded by a Li_2S matrix (formed during the first lithiation), which is consistent with the TEM and XRD results. Figure S10c shows TOF-SIMS depth profiles recorded in positive polarity (O_2^- sputtering) after first charge

DOI: 10.1021/acsnano.6b04214
ACS Nano 2016, 10, 10778−10788

and discharge. The $SnLi^+$ signal (normalized to the Sn^+ signal) of the pristine SnS_2/NRGO electrode was nearly zero throughout the analyzed depth, owing to the absence of the Li_xSn alloys in the pristine electrode. The normalized $SnLi^+$ signal of the delithiated SnS_2/NRGO electrode decreased slowly with sputtering time to a value of 0.3 after 500 s (not zero), which might be attributed to irreversibly deposited Li^+ or electrically detached Li_xSn species from the electrode during discharge and charge. The lithiated SnS_2/NRGO electrode shows an almost 4 times higher $SnLi^+$ normalized total signal compared to the delithiated electrode in the first 500 s of sputtering, revealing that the Sn species in the lithiated electrode are indeed more lithiated; that is, they are Li_xSn alloys. On the basis of the TEM (Figure S9), XRD (Figure S10a), and TOF-SIMS results (Figure S10b and c), the structure of the SnS_2/NRGO electrode in the pristine, lithiated, and delithiated states can be illustrated as shown in Figure S10d.

In Figure 7a, the SnS_2/NRGO maintains a stable capacity for 200 charging−discharging cycles. Its capacity is still 562 mAh g^{-1} at the 200th cycle, and the Coulombic efficiency remains *ca.* 99% after the fifth cycle (Figure S11). From the 10th to 200th cycle, its capacity decay was only 0.07 mAh g^{-1} per cycle, indicating excellent cycling stability. In contrast, the other electrodes showed relatively poor cycling stability. The 200th cycle capacities at 0.2 A g^{-1} are 297, 229, and 75 mAh g^{-1} for the SnS_2, SnS/NRGO, and SnS, respectively. The reversible capacity of the SnS_2/NRGO electrode compares favorably with the previously reported SnS_2-carbon or SnS-carbon composite anodes listed in Table S1.[7,12,13,16−21,34−36,38−47] Figure 7b shows the retained capacity of the four electrodes when cycled at rates up to 5.0 A g^{-1}. The SnS_2/NRGO electrode retains a higher capacity at all of the rates. For example, at 2.0 A g^{-1} it retains a capacity of 402 mAh g^{-1} after 40 cycles; when the current density is returned to 0.2 A g^{-1}, the electrode recovers its initial capacity of 597 mAh g^{-1}. In contrast, the capacities of the SnS and the SnS/NRGO electrodes fade, dropping from above 530 mAh g^{-1} at the 10th cycle to 394 mAh g^{-1} for the SnS and 449 mAh g^{-1} for the SnS/NRGO at the 60th cycle; the capacity of the unsupported SnS_2 electrode also fades, dropping from 576 mAh g^{-1} at the 10th cycle to 509 mAh g^{-1} at the 60th cycle. The SnS_2/NRGO and SnS/NRGO electrodes showed better cycling performance and rate capability compared to their unsupported electrodes, indicating the effective role of the NRGO as a support material. The NRGO could provide good electrical pathways to the loaded tin sulfide nanocrystals and effectively cushion the volume expansion of the Sn metals during charging−discharging cycles. In addition, for all the electrodes, the Li_2S derived from the decomposition of the tin sulfides is an inert phase in the present cutoff voltage range, and thus it might play a role as a buffering matrix to restrain the growth of the Li−Sn alloy during lithiation and delithiation cycles.[9] In fact, metallic Sn without the Li_2S phase faded rapidly in 100 cycles due to the volume expansion and the subsequent pulverization (Figure S11).[33] This observation implies that compared to the metallic Sn electrode, the prepared SnS and SnS_2 (unsupported or NRGO-supported) electrodes showed better cycling stability *via* the aid of the Li_2S matrix.

The electrochemical impedance spectra (EIS) of the four cycled electrodes at 0.2−5.0 A g^{-1} were recorded, and the Nyquist plots are shown in Figure 7c. The data were fit to an equivalent circuit, and the resultant parameters are listed in Table S2. The semicircle in the Nyquist plots originates from

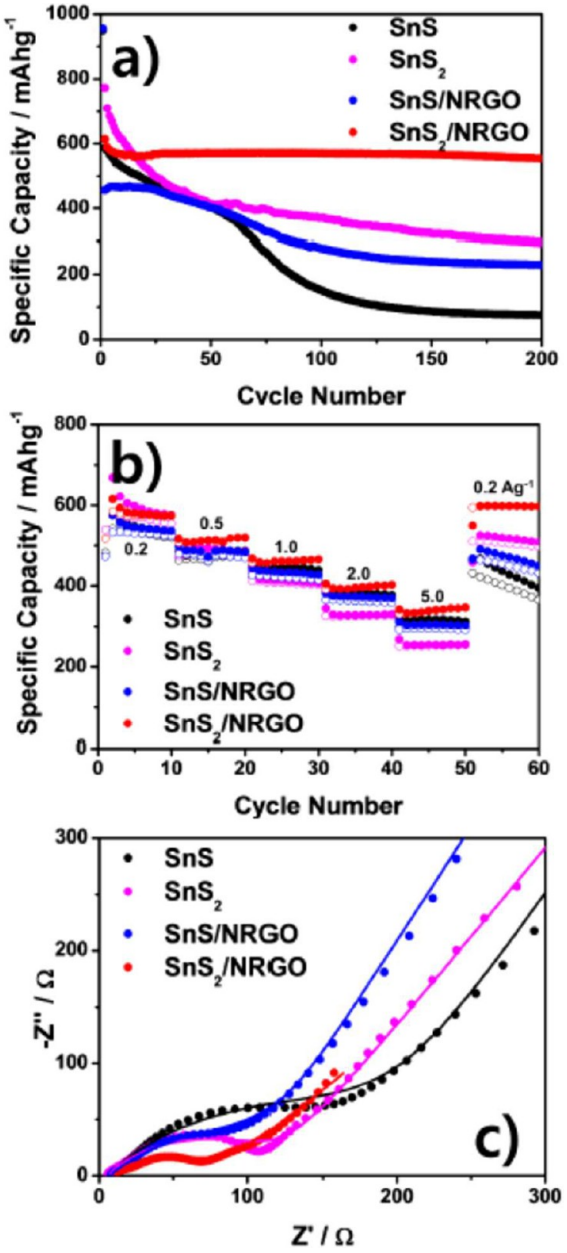

Figure 7. (a) Dependence of the specific capacity on the cycle number at a constant specific current of 0.2 A g^{-1}; (b) dependence of the specific capacity on the specific current; (c) Nyquist plots of SnS, SnS_2, SnS/NRGO, and SnS_2/NRGO.

the charge transfer resistance (R_{ct}) and the corresponding capacitance, which describe the charge transfer process at the interface between the electrode and electrolyte. For the SnS_2/NRGO electrode R_{ct} is the smallest, only 78.0 Ω, well below the R_{ct} of the SnS/NRGO, SnS_2, and SnS electrodes, respectively 166.6 Ω, 128.1 Ω, and 239.6 Ω. The SnS_2/NRGO electrode also has the highest capacitance of 506.9 μF, well above the 299.8 μF capacitance of the electrode made with SnS/NRGO and of unsupported SnS_2 (157.6 μF) or unsupported SnS (144.0 μF). Because the capacitance scales with the electrolyte-accessible area, it is evident that the NRGO greatly increases the accessible area, as expected from the TEM results showing that NRGO arrests the aggregation of the SnS_2 and SnS nanocrystals.

DOI: 10.1021/acsnano.6b04214
ACS Nano 2016, 10, 10778−10788

Model Explaining the Significance of Noncycling Li_2S: Theoretical Ground-State Structures and Voltage Profiles. To better understand the cause of the difference between the performances of the SnS and SnS_2 electrodes, computational simulations were performed carefully examining the role of noncycling Li_2S, the fraction of which is double that in anodes made with SnS_2 compared with anodes made with SnS. Upon lithiation, both SnS and SnS_2 initially form Li_2S *via* the strongly exoergic reactions of eqs 1 and 2.

$$\mathrm{Li} + \frac{1}{4}\mathrm{SnS_2} \rightarrow \frac{1}{2}\mathrm{Li_2S} + \frac{1}{4}\mathrm{Sn} \quad \Delta E = -1.74\ \mathrm{eV} \tag{1}$$

$$\mathrm{Li} + \frac{1}{2}\mathrm{SnS} \rightarrow \frac{1}{2}\mathrm{Li_2S} + \frac{1}{2}\mathrm{Sn} \quad \Delta E = -1.58\ \mathrm{eV} \tag{2}$$

As mentioned earlier, twice as much Li_2S per Sn is formed in SnS_2 as compared to SnS; its greater amount in the SnS_2 anode buffers the volume expansion of 63% as compared to 91% in SnS for the subsequent cycles, in which only the Sn component is active for lithiation (Figure 8).[48] The improved cycle

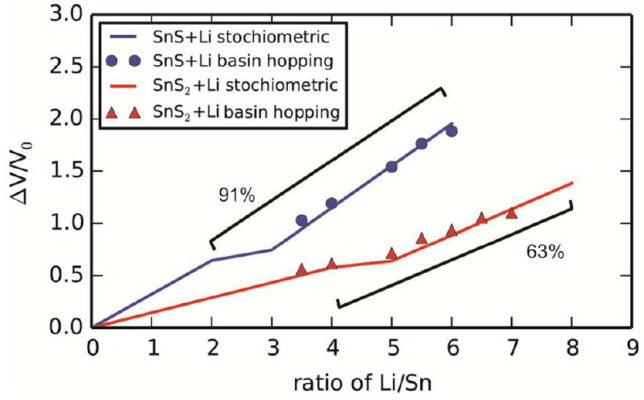

Figure 8. Calculated relative volume changes in the first lithiation half-cycles of SnS (blue) and SnS_2 (red) for basin hopping structures (symbols) and the stoichiometry (lines). The annotated values indicate the relative volume change of each material in the second and subsequent cycles, where only the Sn component is active.

performance seen in SnS_2 is consistent with the consensus linking volume change to capacity fade in alloy systems, *e.g.*, Si, Ge, and Sn, *via* cracking and pulverization of the active material.[49,50] Because of the stability of Li_2S, *i.e.*, its large Gibbs free energy of formation, only Sn is electrochemically active at potentials of less than 1.5 V *versus* Li^+/Li.

The thermodynamics does not reveal by itself the structure of the formed Li_2S.[9,22,35] To identify the stable structures produced in the reactions of eqs 1 and 2, we performed calculations of supercells with the stoichiometry of $(Li_2S)_x$ + Sn, x = 1, 2. The structures were globally optimized using the basin-hopping Monte Carlo algorithm, allowing for optimization of all atomic and cell degrees of freedom. Two starting structures were used in the global optimization, amorphous Li_2S and crystalline Li_2S, combined with Li_xSn with increasing x. The lowest energy, *i.e.*, the most stable, configurations contained layers of Li_2S and Sn in a sandwich structure.

The formation energies of the amorphous and sandwiched structures were calculated as

$$E_{\mathrm{formation}} = \frac{E_{\mathrm{LixSn-Li2S}} - yE_{\mathrm{Sn*}} - xE_{\mathrm{Li}}}{y + x} \tag{4}$$

$$E_{\mathrm{LixSn-Li2S}} = E_{\mathrm{LixSn-Li2S}} - yzE_{\mathrm{Li2S}}$$

where z = 1 indicates SnS and z = 2 indicates SnS_2 stoichiometric equivalents. All sandwich structures were lower in energy than their amorphous counterparts and thus form the convex hull shown in Figure 9a. The amorphous structures of

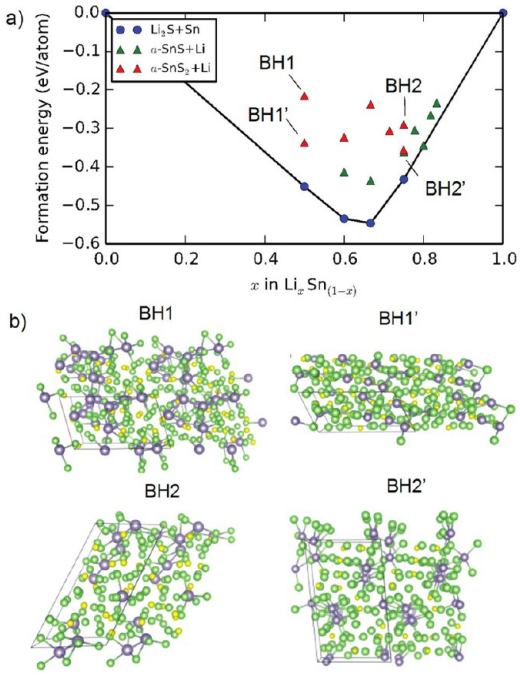

Figure 9. (a) Convex hull formed of structures with Sn sandwiched between crystalline Li_2S layers. The amorphous structures above the hull are thermodynamically unstable. (b) Structures showing that Sn segregation is favorable. Green spheres are Li^+; yellow are S^{2-}; and gray are Sn.

two charging states at the initial (BH1) and final (BH2) low-energy configurations are shown in Figure 9b. The change in configuration along the basin-hopping relaxation from BH1 → BH1′ and BH2 → BH2′ shows that Sn preferentially forms domains with no sulfur neighbors in its first coordination shell. With sufficient sampling, we expect that basin-hopping would eventually find the ordered structures with domains of Sn sandwiched in Li_2S (Figure 10b). Interestingly, the amorphous and ordered structures of the same Li concentration have a similar volume, showing that the volume buffering from the Li_2S phase is insensitive to crystalline Li_2S formation. For simplicity, further calculations of lithiation are based on the most stable crystalline Li_2S–Sn sandwich structure.

Voltages between states of charge in the sandwiched Sn structure were calculated based on the formation energies along the convex hull; the voltage profile is plotted in Figure 10a. Owing to the interface between Li_2S and Sn, the voltage corresponding to the reaction in eq 1 is 1.51 V, lower than the bulk limit, 1.74 V. The following capacity beyond Li/Sn = 4 is reversible for the second and subsequent cycles. The calculated voltage profile is in good agreement with experiment (Figure 6). We have shown the most stable configuration of the Li + SnS_x, x = 1, 2, is similar to Sn domains sandwiched between Li_2S (Figure 10b). From these results, the difference between

DOI: 10.1021/acsnano.6b04214
ACS Nano 2016, 10, 10778–10788

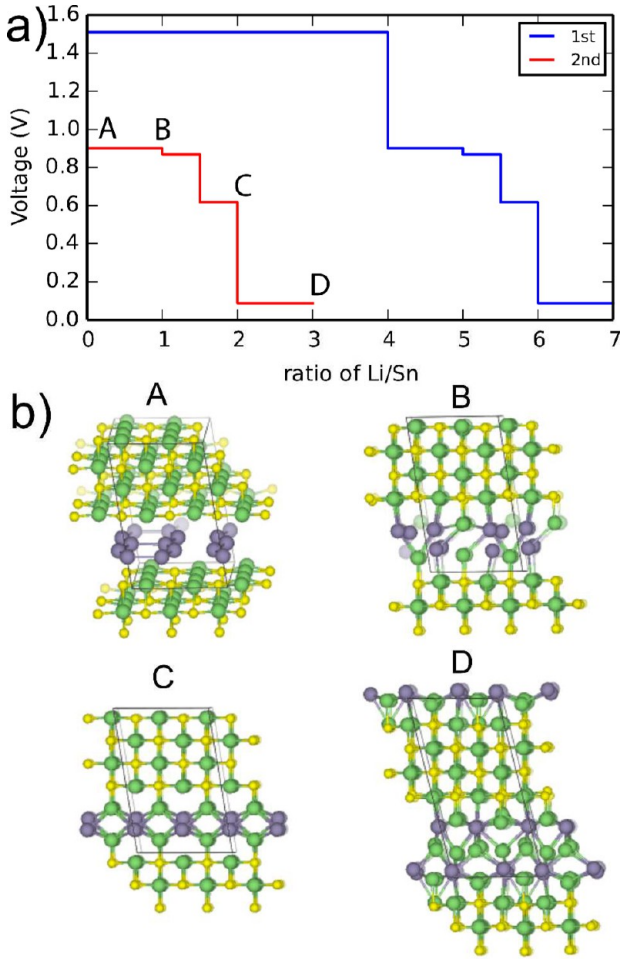

Figure 10. (a) Calculated voltage profiles of the first and second lithiation cycles of the SnS_2. (b) Sandwich structures along the convex hull determining the voltage profile. Green spheres are Li^+; yellow are S^{2-}; and gray are Sn.

the SnS and the SnS_2 is expected to be due to the different quantities of Sn supported by the Li_2S matrix. Half of the Li_2S per Sn is formed for the SnS as compared with the SnS_2, and the Sn domains in SnS suffer from a greater relative volume expansion and thus lower cycling stability. We argue, therefore, that the presence of the Li_2S matrix increases the cycling stability of the Sn anode by supporting the Sn in domains, buffering the volume expansion, and reducing crack formation and failure in the Sn component.

Starting from a sandwiched Li_2S + $Li_{3.5}Sn$ structure, we explored possible mechanisms for Li diffusion using molecular dynamics (MD) simulations at 450 K. Several diffusion events involving one or multiple Li atoms were found over the course of a 10 ps trajectory. The reaction mechanisms were categorized as occurring either at or away from the Li_2S/$Li_{3.5}Sn$ interface. In all hopping events, Li diffusion initiated from sites where Li−S and/or Li−Sn bonding was frustrated by either over- or undercoordination. Low diffusion barriers of <0.1 eV were found for Li diffusion at the Li_2S/$Li_{3.5}Sn$ interface, whereas larger barriers, ∼0.30 eV, had to be overcome for Li diffusion in the $Li_{3.5}Sn$ phase. In all high-barrier mechanisms, there was concerted motion of multiple Li atoms. Examples of these low- and high-barrier mechanisms are shown in Figure 11. From these simulations we conclude that facile Li diffusion is achieved primarily by multiple fast hops along the Li_2S/$Li_{3.5}Sn$ interface with slower diffusion through the $Li_{3.5}Sn$ domain. In contrast to a pure Li−Sn system, which has hopping barriers of 0.45 eV, Li diffusion in the Li_2S + Li_xSn system is expected to be significantly faster.

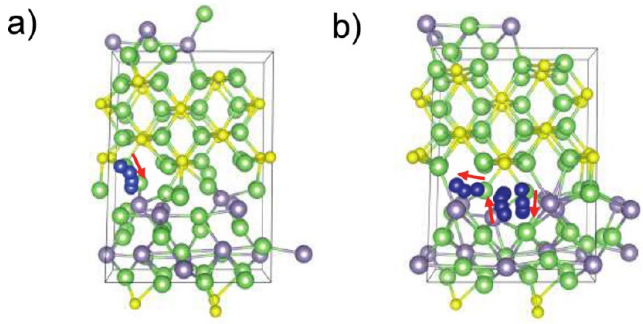

Figure 11. Mechanism of Li^+ diffusion (a) for a < 0.1 eV barrier at the Li_2S/$Li_{35}Sn$ interface and (b) for a 0.3 eV barrier within a $Li_{3.5}Sn$ crystallite. Blue spheres and red arrows show exemplary Li^+ paths.

CONCLUSIONS

The noncycling Li_2S and nitrogen-doped reduced graphene oxide substrates are of essence for the capacity retention of Li-alloyed/dealloyed Sn nanoparticle electrodes. As recognized earlier, they reduce the volume fraction of the lithiated/delithiated tin, and they limit the mechanical stress associated with the expansion upon lithiation and shrinkage upon delithiation. They also have, however, other essential functions. NRGO sheets not only improve the electronic conductivity but are substrates on which nonaggregating SnS and SnS_2 nanocrystals form. Electrolyte-accessible, *i.e.*, Li^+ accessible, nonaggregating electroactive Sn nanoparticles form when NRGO-supported SnS and SnS_2 nanocrystals are electro-reduced. The Li_2S nanodomains not only prevent excessive stress but also form Sn nanodomain interphases in which lithium percolates rapidly. For these reasons, SnS_2, which provides twice the Li_2S provided by SnS, cycles better, and NRGO massively improves the cycling of both SnS and SnS_2. The winner is consequently NRGO-supported SnS_2. When cycling at a specific rate of 0.2 A g^{-1}, it retains at the 200th cycle a Coulombic capacity of 562 mAh g^{-1}, only slightly less than its 10th cycle capacity of 597 mAh g^{-1}.

METHODS

Syntheses of SnS/NRGO and SnS_2/NRGO. Graphite oxide, prepared by Hummer's method,[51] was dispersed in 15 mL of ethanol. Then 1.0 g of $SnCl_4$ dissolved in 2.5 mL of ethanol was added, followed by 584.3 mg of solid thiourea. After stirring for 1 h, the mixture was heated for 3 h under argon to a temperature between 450 and 750 °C. SnS and SnS_2 without GO were similarly prepared, the SnS_2 by heating to 450 °C and the SnS by heating to 650 °C.

Characterization. X-ray diffraction patterns were obtained with a Rigaku R-axis Spider. A Quanta FEG 650 scanning electron microscope was used for imaging and energy dispersive spectra; a JEOL JEM-2010F high-resolution transmission electron microscope was used for the TEM. X-ray photoelectron spectra were obtained with a Kratos Axis Ultra DLD. Raman spectra were obtained with a Witec Alpha 300. Thermogravimetric analyses (TGA) were performed with a Mettler-Toledo TGA/DSC1 with air flowing over the samples heated at 10/min. TOF-SIMS depth profiles were collected using an ION-TOF GmbH TOF.SIMS 5 equipped with a pulsed (20 ns) Bi_1^+ analysis ion beam at 30 keV ion energy. For depth profiling Cs^+ (500 eV ion energy) and O_2^- (1 keV ion energy) sputtering beams were

DOI: 10.1021/acsnano.6b04214
ACS Nano 2016, 10, 10778−10788

employed for negative and positive secondary ion polarity measurements, respectively.

Electrochemical Measurements. The SnS/NRGO and SnS_2/NRGO composites was dispersed in water with 90 kDa carboxymethyl cellulose binder (Aldrich) and Super P−Li carbon to produce a 6:2:2 weight ratio slurry of solids. The slurry was coated on a Cu foil using a notch bar and dried at 80 °C for 12 h in a vacuum oven. The mass loading was 0.8−1.0 mg cm^{-2}. Coin cells were fabricated using a lithium foil as counter and reference electrode, a polypropylene membrane (Celgard 2400) separator, and 1.0 M $LiPF_6$ in ethylene carbonate/diethyl carbonate (1:1 v/v) electrolyte. The cells were galvanostatically charged/discharged using a battery tester (Arbin, BT 2143). The measured potential range was 0.01−1.3 V. Electrochemical impedance spectra were measured through the 10^5 to 10^{-1} Hz range with a modulation amplitude of 5 mV using a potentiostat (CHI 608D, CH Instruments). The EIS spectra were fit with Z-view software.

Computational Simulations. The basin-hopping algorithm[52] was used to find low-energy structures starting from random configurations of SnS_x + Li (x = 1, 2) as well as global minima consisting of sandwiched Sn and Li_2S layers. Cells were constructed with eight unit cells of SnS_x (x = 1, 2), and supercells were allowed to relax in all degrees of freedom for each nominal amount of Li added. Ab initio molecular dynamics was run to search for Li hopping mechanisms in a Li_2S + $Li_{3.5}Sn$ cell sandwich configuration. A time step of 2 fs was used for the integration, and the temperature was controlled by velocity rescaling every 20 time steps. MD was run at 450 K for 40 ps to equilibrate, then 10 ps for data collection. Configurations along the 10 ps trajectory were minimized after subsequent Li hopping events, and the nudged elastic band method (NEB) was used to find energy barriers along the transition pathway.[53,54]

All energies were calculated with density function theory as implemented in the Vienna ab initio simulation package.[55] The projector-augmented wave framework was used to describe the core electrons.[56,57] Valence electrons were described by single-electron Kohn−Sham wave functions[58,59] that were expanded in a plane-wave basis set up to a kinetic energy cutoff of 260 eV during basin-hopping searches and 333 eV for relaxations of the minima forming the convex hull construction. The generalized gradient approximation with the PBE functional was used to describe electronic correlation and exchange.[60] Gaussian-type smearing with a width of 0.05 eV around the Fermi level was used to improve convergence. All systems were optimized to their ground-state geometry until the forces on each atom were less than 0.01 eV/Å. The Brillouin zone was sampled with a 1 × 1 × 1 k-point mesh for basin-hopping and a 3 × 3 × 3 Monkhorst−Pack grid of k points for final relaxations and the NEB calculations.[61]

ASSOCIATED CONTENT

Supporting Information

The Supporting Information is available free of charge on the ACS Publications website at DOI: 10.1021/acsnano.6b04214.

XRD, SEM, XPS, TGA, and EIS results of the sample (PDF)

AUTHOR INFORMATION

Corresponding Author

*E-mail: mullins@che.utexas.edu.

ORCID

Graeme Henkelman: 0000-0002-0336-7153

Notes

The authors declare no competing financial interest.

ACKNOWLEDGMENTS

This work was supported by the Welch Foundation through grants F-1131 (A.H.), F-1841 (G.H.), and F-1436 (C.B.M.) as well as the National Science Foundation grant number CBET-1603491 (C.B.M.). D.H.Y. thanks Wontae Joo, Dr. Karalee Jarvis, and Dr. Hugo Celio for experimental assistance and for helpful conversations. We also acknowledge the NSF grant DMR-0923096 used to purchase the TOF-SIMS instrument in the Texas Materials Institute.

REFERENCES

(1) Scrosati, B.; Garche, J. Lithium Batteries: Status, Prospects and Future. *J. Power Sources* **2010**, *195*, 2419−2430.

(2) Choi, N.-S.; Chen, Z.; Freunberger, S. A.; Ji, X.; Sun, Y.-K.; Amine, K.; Yushin, G.; Nazar, L. F.; Cho, J.; Bruce, P. G. Challenges Facing Lithium Batteries and Electrical Double-Layer Capacitors. *Angew. Chem., Int. Ed.* **2012**, *51*, 9994−10024.

(3) Youn, D. H.; Patterson, N. A.; Park, H.; Heller, A.; Mullins, C. B. Facile Synthesis of Ge/N-Doped Carbon Spheres with Varying Nitrogen Content for Lithium Ion Battery Anodes. *ACS Appl. Mater. Interfaces* **2016**, *8*, 27788−27794.

(4) Zeng, G.; Shi, N.; Hess, M.; Chen, X.; Cheng, W.; Fan, T.; Niederberger, M. A General Method of Fabricating Flexible Spinel-Type Oxide/Reduced Graphene Oxide Nanocomposite Aerogels as Advanced Anodes for Lithium-Ion Batteries. *ACS Nano* **2015**, *9*, 4227−4235.

(5) Chang, K.; Geng, D.; Li, X.; Yang, J.; Tang, Y.; Cai, M.; Li, R.; Sun, X. Ultrathin MoS_2/Nitrogen-Doped Graphene Nanosheets with Highly Reversible Lithium Storage. *Adv. Energy Mater.* **2013**, *3*, 839−844.

(6) Chang, K.; Chen, W. l-Cysteine-Assisted Synthesis of Layered MoS_2/Graphene Composites with Excellent Electrochemical Performances for Lithium Ion Batteries. *ACS Nano* **2011**, *5*, 4720−4728.

(7) Seo, J.-W.; Jang, J.-T.; Park, S.-W.; Kim, C.; Park, B.; Cheon, J. Two-Dimensional SnS_2 Nanoplates with Extraordinary High Discharge Capacity for Lithium Ion Batteries. *Adv. Mater.* **2008**, *20*, 4269−4273.

(8) Youn, D. H.; Jo, C.; Kim, J. Y.; Lee, J.; Lee, J. S. Ultrafast synthesis of MoS_2 or WS_2-Reduced Graphene Oxide Composites *via* Hybrid Microwave Annealing for Anode Materials of Lithium Ion Batteries. *J. Power Sources* **2015**, *295*, 228−234.

(9) Li, Y.; Tu, J. P.; Huang, X. H.; Wu, H. M.; Yuan, Y. F. Nanoscale SnS with and without Carbon-Coatings as an Anode Material for Lithium Ion Batteries. *Electrochim. Acta* **2006**, *52*, 1383−1389.

(10) Im, H. S.; Cho, Y. J.; Lim, Y. R.; Jung, C. S.; Jang, D. M.; Park, J.; Shojaei, F.; Kang, H. S. Phase Evolution of Tin Nanocrystals in Lithium Ion Batteries. *ACS Nano* **2013**, *7*, 11103−11111.

(11) Xu, X.; Liu, W.; Kim, Y.; Cho, J. Nanostructured Transition Metal Sulfides for Lithium Ion Batteries: Progress and Challenges. *Nano Today* **2014**, *9*, 604−630.

(12) Wu, P.; Du, N.; Zhang, H.; Liu, J.; Chang, L.; Wang, L.; Yang, D.; Jiang, J.-Z. Layer-Stacked Tin Disulfide Nanorods in Silica Nanoreactors with Improved Lithium Storage Capabilities. *Nanoscale* **2012**, *4*, 4002−4006.

(13) Mukaibo, H.; Yoshizawa, A.; Momma, T.; Osaka, T. Particle Size and Performance of SnS_2 Anodes for Rechargeable Lithium Batteries. *J. Power Sources* **2003**, *119*, 60−63.

(14) He, M.; Yuan, L.-X.; Huang, Y.-H. Acetylene Black Incorporated Three-Dimensional Porous SnS_2 Nanoflowers with High Performance for Lithium Storage. *RSC Adv.* **2013**, *3*, 3374−3383.

(15) Kang, J.-G.; Lee, G.-H.; Park, K.-S.; Kim, S.-O.; Lee, S.; Kim, D.-W.; Park, J.-G. Three-Dimensional Hierarchical Self-Supported Multi-Walled Carbon Nanotubes/Tin(iv) Disulfide Nanosheets Heterostructure Electrodes for High Power Li Ion Batteries. *J. Mater. Chem.* **2012**, *22*, 9330−9337.

(16) Luo, B.; Fang, Y.; Wang, B.; Zhou, J.; Song, H.; Zhi, L. Two Dimensional Graphene-SnS_2 Hybrids with Superior Rate Capability for Lithium Ion Storage. *Energy Environ. Sci.* **2012**, *5*, 5226−5230.

(17) Sathish, M.; Mitani, S.; Tomai, T.; Honma, I. Ultrathin SnS_2 Nanoparticles on Graphene Nanosheets: Synthesis, Characterization, and Li-Ion Storage Applications. *J. Phys. Chem. C* **2012**, *116*, 12475−12481.

DOI: 10.1021/acsnano.6b04214
ACS Nano 2016, 10, 10778−10788

(18) Liu, S.; Lu, X.; Xie, J.; Cao, G.; Zhu, T.; Zhao, X. Preferential c-Axis Orientation of Ultrathin SnS_2 Nanoplates on Graphene as High-Performance Anode for Li-Ion Batteries. *ACS Appl. Mater. Interfaces* **2013**, *5*, 1588−1595.
(19) Tao, H.-C.; Yang, X.-L.; Zhang, L.-L.; Ni, S.-B. One-Step *in situ* Synthesis of SnS/Graphene Nanocomposite with Enhanced Electrochemical Performance for Lithium Ion Batteries. *J. Electroanal. Chem.* **2014**, *728*, 134−139.
(20) Zhu, S.-C.; Tao, H.-C.; Yang, X.-L.; Zhang, L.-L.; Ni, S.-B. Synthesis of N-Doped Graphene/SnS Composite and Its Electrochemical Properties for Lithium Ion Batteries. *Ionics* **2015**, *21*, 2735−2742.
(21) Li, S.; Zheng, J.; Zuo, S.; Wu, Z.; Yan, P.; Pan, F. 2D Hybrid Anode Based on SnS Nanosheet Bonded with Graphene to Enhance Electrochemical Performance for Lithium-Ion Batteries. *RSC Adv.* **2015**, *5*, 46941−46946.
(22) Gou, X.-L.; Chen, J.; Shen, P.-W. Synthesis, Characterization and Application of SnS_x (x = 1, 2) Nanoparticles. *Mater. Chem. Phys.* **2005**, *93*, 557−566.
(23) Yang, J.; Zeng, J.-h.; Yu, S.-H.; Yang, L.; Zhang, Y.-H.; Qian, Y.-T. Pressure-Controlled Fabrication of Stibnite Nanorods by the Solvothermal Decomposition of a Simple Single-Source Precursor. *Chem. Mater.* **2000**, *12*, 2924−2929.
(24) Thongtem, T.; Phuruangrat, A.; Thongtem, S. Synthesis and Analysis of CuS with Different Morphologies Using Cyclic Microwave Irradiation. *J. Mater. Sci.* **2007**, *42*, 9316−9323.
(25) Pei, S.; Cheng, H.-M. The Reduction of Graphene Oxide. *Carbon* **2012**, *50*, 3210−3228.
(26) Youn, D. H.; Jang, J.-W.; Kim, J. Y.; Jang, J. S.; Choi, S. H.; Lee, J. S. Fabrication of Graphene-Based Electrode in Less Than a Minute Through Hybrid Microwave Annealing. *Sci. Rep.* **2014**, *4*, 5492.
(27) Zhou, T.; Pang, W. K.; Zhang, C.; Yang, J.; Chen, Z.; Liu, H. K.; Guo, Z. Enhanced Sodium-Ion Battery Performance by Structural Phase Transition from Two-Dimensional Hexagonal-SnS_2 to Orthorhombic-SnS. *ACS Nano* **2014**, *8*, 8323−8333.
(28) Qu, B.; Ma, C.; Ji, G.; Xu, C.; Xu, J.; Meng, Y. S.; Wang, T.; Lee, J. Y. Layered SnS_2-Reduced Graphene Oxide Composite − A High-Capacity, High-Rate, and Long-Cycle Life Sodium-Ion Battery Anode Material. *Adv. Mater.* **2014**, *26*, 3854−3859.
(29) Li, Y.; Wang, H.; Xie, L.; Liang, Y.; Hong, G.; Dai, H. MoS_2 Nanoparticles Grown on Graphene: An Advanced Catalyst for the Hydrogen Evolution Reaction. *J. Am. Chem. Soc.* **2011**, *133*, 7296−7299.
(30) Ferrari, A. C.; Robertson, J. Interpretation of Raman Spectra of Disordered and Amorphous Carbon. *Phys. Rev. B: Condens. Matter Mater. Phys.* **2000**, *61*, 14095−14107.
(31) Cui, P.; Lee, J.; Hwang, E.; Lee, H. One-Pot Reduction of Graphene Oxide at Subzero Temperatures. *Chem. Commun.* **2011**, *47*, 12370−12372.
(32) Stankovich, S.; Dikin, D. A.; Piner, R. D.; Kohlhaas, K. A.; Kleinhammes, A.; Jia, Y.; Wu, Y.; Nguyen, S. T.; Ruoff, R. S. Synthesis of Graphene-Based Nanosheets *via* Chemical Reduction of Exfoliated Graphite Oxide. *Carbon* **2007**, *45*, 1558−1565.
(33) Youn, D. H.; Heller, A.; Mullins, C. B. Simple Synthesis of Nanostructured Sn/Nitrogen-Doped Carbon Composite Using Nitrilotriacetic Acid as Lithium Ion Battery Anode. *Chem. Mater.* **2016**, *28*, 1343−1347.
(34) Chang, K.; Wang, Z.; Huang, G.; Li, H.; Chen, W.; Lee, J. Y. Few-layer SnS_2/Graphene Hybrid with Exceptional Electrochemical Performance as Lithium-Ion Battery Anode. *J. Power Sources* **2012**, *201*, 259−266.
(35) Ji, L.; Xin, H. L.; Kuykendall, T. R.; Wu, S.-L.; Zheng, H.; Rao, M.; Cairns, E. J.; Battaglia, V.; Zhang, Y. SnS_2 Nanoparticle Loaded Graphene Nanocomposites for Superior Energy Storage. *Phys. Chem. Chem. Phys.* **2012**, *14*, 6981−6986.
(36) Kang, J.-G.; Park, J.-G.; Kim, D.-W. Superior Rate Capabilities of SnS Nanosheet Electrodes for Li Ion Batteries. *Electrochem. Commun.* **2010**, *12*, 307−310.
(37) Jeon, B. H.; Yeon, J. H.; Kim, K. M.; Chung, I. J. Preparation and Electrochemical Properties of Lithium−Sulfur Polymer Batteries. *J. Power Sources* **2002**, *109*, 89−97.
(38) Jiang, Z.; Wang, C.; Du, G.; Zhong, Y. J.; Jiang, J. Z. *In Situ* Synthesis of SnS_2@Graphene Nanocomposites for Rechargeable Lithium Batteries. *J. Mater. Chem.* **2012**, *22*, 9494−9496.
(39) Lu, J.; Nan, C.; Li, L.; Peng, Q.; Li, Y. Flexible SnS Nanobelts: Facile Synthesis, Formation Mechanism and Application in Li-Ion Batteries. *Nano Res.* **2013**, *6*, 55−64.
(40) Zhang, M.; Lei, D.; Yu, X.; Chen, L.; Li, Q.; Wang, Y.; Wang, T.; Cao, G. Graphene Oxide Oxidizes Stannous Ions to Synthesize Tin Sulfide-Graphene Nanocomposites with Small Crystal Size for High Performance Lithium Ion Batteries. *J. Mater. Chem.* **2012**, *22*, 23091−23097.
(41) Zhuo, L.; Wu, Y.; Wang, L.; Yu, Y.; Zhang, X.; Zhao, F. One-Step Hydrothermal Synthesis of SnS_2/Graphene Composites as Anode Material for Highly Efficient Rechargeable Lithium Ion Batteries. *RSC Adv.* **2012**, *2*, 5084−5087.
(42) Guan, D.; Li, J.; Gao, X.; Xie, Y.; Yuan, C. Growth Characteristics and Influencing Factors of 3D Hierarchical Flower-Like SnS_2 Nanostructures and Their Superior Lithium-Ion Intercalation Performance. *J. Alloys Compd.* **2016**, *658*, 190−197.
(43) Deng, W.; Chen, X.; Liu, Z.; Hu, A.; Tang, Q.; Li, Z.; Xiong, Y. Three-Dimensional Structure-Based Tin Disulfide/Vertically Aligned Carbon Nanotube Arrays Composites as High-Performance Anode Materials for Lithium Ion Batteries. *J. Power Sources* **2015**, *277*, 131−138.
(44) Shen, C.; Ma, L.; Zheng, M.; Zhao, B.; Qiu, D.; Pan, L.; Cao, J.; Shi, Y. Synthesis and Electrochemical Properties of Graphene-SnS_2 Nanocomposites for Lithium-Ion Batteries. *J. Solid State Electrochem.* **2012**, *16*, 1999−2004.
(45) Yin, J.; Cao, H.; Zhou, Z.; Zhang, J.; Qu, M. SnS_2@Reduced Graphene Oxide Nanocomposites as Anode Materials with High Capacity for Rechargeable Lithium Ion Batteries. *J. Mater. Chem.* **2012**, *22*, 23963−23970.
(46) Jin, H.; Gu, M.; Ji, S.; Xu, X.; Liu, J. Reduced Graphene Oxide Anchored Tin Sulfide Hierarchical Microspheres with Superior Li-Ion Storage Performance. *Ionics* **2016**, *22*, 1811−1818.
(47) Ma, Z.; Wang, Y.; Yang, Y.; Yousaf, M.; Zou, M.; Cao, A.; Han, R. P. S. Flexible Hybrid Carbon Nanotube Sponges Embedded with SnS_2 from Tubular Nanosheaths to Nanosheets as Free-Standing Anodes for Lithium-Ion Batteries. *RSC Adv.* **2016**, *6*, 30098−30105.
(48) Brousse, T.; Lee, S. M.; Pasquereau, L.; Defives, D.; Schleich, D. M. Composite Negative Electrodes for Lithium Ion Cells. *Solid State Ionics* **1998**, *113*−*115*, 51−56.
(49) Obrovac, M. N.; Chevrier, V. L. Alloy Negative Electrodes for Li-Ion Batteries. *Chem. Rev.* **2014**, *114*, 11444−11502.
(50) McDowell, M. T.; Lee, S. W.; Nix, W. D.; Cui, Y. Understanding the Lithiation of Silicon and Other Alloying Anodes for Lithium-Ion Batteries. *Adv. Mater.* **2013**, *25*, 4966−4985.
(51) Hummers, W. S.; Offeman, R. E. Preparation of Graphitic Oxide. *J. Am. Chem. Soc.* **1958**, *80*, 1339−1339.
(52) Wales, D. J.; Doye, J. P. K. Global Optimization by Basin-Hopping and the Lowest Energy Structures of the Lennard-Jones Clusters Containing Up to 110 Atoms. *J. Phys. Chem. A* **1997**, *101*, 5111−5116.
(53) Henkelman, G.; Uberuaga, B. P.; Jonsson, H. A Climbing Image Nudged Elastic Band Method for Finding Saddle Points and Minimum Energy Paths. *J. Chem. Phys.* **2000**, *113*, 9901−9904.
(54) Henkelman, G.; Jonsson, H. Improved Tangent Estimate in the Nudged Elastic Band Method for Finding Minimum Energy Paths and Saddle Points. *J. Chem. Phys.* **2000**, *113*, 9978−9985.
(55) Kresse, G.; Hafner, J. *Ab Initio* Molecular Dynamics for Liquid Metals. *Phys. Rev. B: Condens. Matter Mater. Phys.* **1993**, *47*, R558−R561.
(56) Hohenberg, P.; Kohn, W. Inhomogeneous Electron Gas. *Phys. Rev.* **1964**, *136*, 864−871.
(57) Kohn, W.; Sham, L. J. Self-Consistent Equations Including Exchange and Correlation Effects. *Phys. Rev.* **1965**, *140*, 1133−1138.

DOI: 10.1021/acsnano.6b04214
ACS Nano 2016, 10, 10778−10788

(58) Blöchl, P. E. Projector Augmented-Wave Method. *Phys. Rev. B: Condens. Matter Mater. Phys.* **1994**, *50*, 17953−17979.
(59) Kresse, G.; Joubert, D. From Ultrasoft Pseudopotentials to the Projector Augmented-Wave Method. *Phys. Rev. B: Condens. Matter Mater. Phys.* **1999**, *59*, 1758−1775.
(60) Perdew, J. P.; Burke, K.; Ernzerhof, M. Generalized Gradient Approximation Made Simple. *Phys. Rev. Lett.* **1996**, *77*, 3865.
(61) Monkhorst, H.; Pack, J. Special Points for The Brillouin-Zone Integrations. *Phys. Rev. B* **1976**, *13*, 5188.

DOI: 10.1021/acsnano.6b04214
ACS Nano 2016, 10, 10778−10788